# Heat and Mass Transport from Neutrally Suspended Oblate Spheroid in Simple Shear Flow

Yanxing Wang<sup>1,\*</sup>, Hui Wan<sup>2</sup>, Ruben Gonzalez Pizarro<sup>1</sup>, Seokbin Lim<sup>3</sup>, and Fangjun Shu<sup>1</sup>,

<sup>1</sup>Department of Mechanical and Aerospace Engineering, New Mexico State University, Las Cruces, NM 88011, USA

<sup>2</sup>Department of Mechanical and Aerospace Engineering, University of Colorado, Colorado Springs, CO 80918, USA

<sup>3</sup>Department of Mechanical Engineering, New Mexico Institute of Mining and Technology, Socorro, NM 87801, USA

Through high-fidelity numerical simulation based on the lattice Boltzmann method, we have conducted an in-depth study on the heat and mass transport from an oblate spheroid neutrally suspended in a simple shear flow. In the simulation, the temperature and mass concentration are modeled as a passive scalar released at the spheroid's surface. The fluid dynamics induced by the interaction of the carrier fluid and the suspended spheroid, as well as the resultant scalar transport process, have been extensively investigated. A coupled transport mechanism comprising several components of the flow around the oblate spheroid has been identified. The effects of Reynolds number and the aspect ratio of the spheroid on the flow characteristics and scalar transport rate are examined. The variation of the nondimensional scalar transport rate suggests that the effect of spheroid shape on scalar transfer rate can be decoupled from the effects of Peclet and Reynolds numbers, which facilitates the development of a correlation of scalar transfer rate for oblate spheroids based on the well-developed correlations for a sphere.

<sup>\*</sup>yxwang@nmsu.edu

## 1. Introduction

Heat and mass transport from neutrally suspended solid particles in shear flows have fundamental importance in both scientific and industrial applications, from traditional drug delivery<sup>1</sup> and metal ore heap leaching<sup>2</sup> to emerging renewable biomass energy<sup>3</sup> and dissolvable microrobots<sup>4</sup>. At the small Prandtl (Pr) and Schmidt (Sc) numbers, heat and mass diffusion play a dominant role in the transport processes. A large number of studies on diffusion-based transport processes have been carried out, and many analytical and theoretical models have been developed and widely used<sup>5-7</sup>. In many applications, such as the dissolution of drug particles, the Schmidt number for the diffusion of drug molecules in water can be up to  $O(10^4)^8$ . Under this condition, the diffusive transport of the molecules becomes inefficient, and the effect of hydrodynamics becomes important. The interaction between the ambient fluid and the suspended particles induces complex hydrodynamics, which in turn create an additional heat and mass transport mechanism. The hydrodynamics are composed of the convection due to the relative velocity between the particle and the surrounding fluid and the flow shear due to the relative motion of adjacent flow layers. It was found by Wang and Brasseur<sup>9</sup> that flow shear plays a more important role in mass transport for small particles. The particle's spinning motion creates a local recirculating flow, which helps advect dissolved mass away from the particle surface.

In nondimensional form the transfer rates are described by Nusselt number (Nu) for heat and Sherwood number (Sh) for mass, which are defined respectively as the ratios of the advective heat and mass transfer rates to diffusive transfer rate. In the situations with fixed temperature or species concentration on the particle surface, the Nusselt and Sherwood numbers are determined by the Reynolds (Re) and Peclet (Pe, which is equal to RePr or ReSc) numbers, defined based on the particle size and flow shear rate. Since the 1960's, considerable effort has been put into the characterization of the heat and mass transfer from spherical particles, and the construction of the dependence of Nu and Sh on Re and Pe. Frankel and Acrivos<sup>10</sup> derived an asymptotic formula for the Sherwood number in terms of the Peclet number in the

limit of  $Pe \rightarrow 0$  at Re = 0 as  $Sh = 1 + 0.257Pe^{1/2}$ . For large Peclet numbers, Acrivos<sup>11</sup> took advantage of the analogy between the sphere and the cylinder in a simple shear flow, and solved the transfer problem using an approximate method. He found that the freely suspended sphere is completely surrounded by a region of closed streamlines at Re = 0, across which heat and mass can only be transferred by diffusion, thereby making the Nu or Sh asymptotically approach a constant ( $\approx 4.5$ ) as Pe goes to infinity. Batchelor<sup>12</sup> followed these important works with an extensive analysis of the transfer rate of heat or mass from a suspended particle in a steady flow with linear velocity distribution in the limit of  $Pe \ll 1$  and  $Pe \gg 1$ . He derived the same asymptotic equation as Frankel and Acrivos<sup>10</sup>, but with a different proportionality constant. The theoretical studies mentioned above established the basis for subsequent studies on this subject. Using an advanced method of asymptotic interpolation on a prescribed form of the formula for Sh and Pe, Polyanin and Dil'man<sup>13</sup> obtained an approximate formula for the Sherwood number over the entire range of Peclet number at Re = 0. Subramanian and Koch<sup>14, 15</sup> proved that the flow inertia caused by non-zero Reynolds number breaks the closed streamlines around the particle in a simple shear flow, and creates an additional mechanism of heat and mass transfer from the particle. They derived a correlation of Sh as a function of Re and Pe, which is applicable in the asymptotic limits of Re  $\ll 1$  and Re  $\gg 1/Pe^{2/5}$ . Due to the intrinsic complexity of transport problems, however, these purely theoretical studies cannot effectively deal with the effect of Reynolds number, and do not provide a good prediction of Nusselt and Sherwood numbers at finite Reynolds numbers.

With the rapid development of computational fluid dynamics methods in recent decades, large-scale numerical simulation now enables the in-depth study of heat and mass transport around moving particles under a wide range of flow conditions. The published studies on flow-shear-driven enhancement of heat and mass transport from spherical particles are still, however, very sparse. A numerical model based on the lattice Boltzmann method based was developed by Wang and Brasseur<sup>9</sup>; they extensively analyzed the hydrodynamic enhancement of heat and mass release from a spherical particle suspended in a simple shear flow, with Reynolds numbers up to 10 and Schmidt numbers up to 100. Based on numerical results, they

developed an accurate correlation for shear enhancement of Nusselt or Sherwood number as a function of Reynolds and Peclet numbers.

In realistic applications, more than 70% of solid particles are believed to be non-spherical, and morphology plays a key role in particle scale heat and mass transfer characteristics  $^{16, 17}$ . Furthermore, non-spherical particles present some interesting characteristics and behaviors, such as good margination in shear flow, that make them broadly useful in bioparticle separation  $^{18}$  and drug delivery  $^{19}$ . As a simplified model of non-spherical particles, the rotational dynamics of a single spheroidal, i.e. oblate or prolate, particle, freely suspended in a shear flow, have been extensively investigated since the 1920's, and several distinctive states have been identified, depending on Reynolds number and particle aspect ratio  $^{20-25}$ . In the past decade, the effects of fluid and particle inertia have become the focus of research. Using lattice-Boltzmann-based numerical methods, Mao and Alexeev  $^{24}$  and Rosén et al.  $^{25}$  independently examined the effects of fluid inertia and particle rotary inertia on the dynamics and trajectory of spheroid particles at low and moderate Reynolds numbers. They found that the particle behaviors are significantly influenced by particle inertia which is characterized by Stokes number (St). Through theoretical analysis, Marath and Subramanian  $^{26, 27}$  systematically studied the effects of fluid and particle inertia on the rotational dynamics of oblate and prolate spheroids, and analyzed the dependence of particle orientation and rotation period on Reynolds and Stokes numbers.

Despite the considerable efforts devoted to the rotational dynamics of oblate and prolate spheroids, however, the mechanisms for heat and mass transport induced by the interaction of carrier fluid and suspended non-spherical particles under shear conditions are still not well understood. In the case where Peclet number is significantly greater than 1, the fluid and particle dynamics play an important role in transporting heat and mass through advection, which combines with diffusion transport to form a coupled transport mechanism. Understanding the fluid dynamics of the interaction between the carrier fluid and the suspended particles is the key to revealing the advective transport mechanism for heat and mass.

Compared with prolate spheroids, the motion of oblate spheroids is relatively simple. Qi and Luo<sup>22</sup> found that in the low Reynolds number range  $0 < Re < Re_c \approx 220$ , the oblate spheroid tends to spin at a

constant speed about its minor axis, where  $Re_c$  is a critical Reynolds number. These conclusions have since been confirmed by other studies<sup>28-30</sup>. As an initial exploration of the complex transport mechanisms in non-spherical particle systems, therefore, this paper focuses on the heat and mass transport from a single oblate spheroid neutrally suspended in a simple shear flow. The primary goal is to identify the complex transport mechanisms of non-spherical particles. To this end, we develop a high-fidelity numerical model based on the multigrid lattice Boltzmann framework, and we extensively examine the transport process of a passive scalar from a neutrally suspended oblate spheroid. We consider spheroids of various aspect ratios in the ranges of  $Re \le 1$  and  $Pe \le 100$ . The paper is organized as follows. The physical model is presented in Section 2. The numerical methods are described in Section 3. The result validation is given in Section 4. The results are analyzed in Section 5, and conclusions are presented in Section 6.

# 2. Physical Model

The surface of a spheroid is described by

$$\frac{xr^2}{a^2} + \frac{yr^2}{b^2} + \frac{zr^2}{c^2} = 1 \tag{1}$$

where a, b and c denote the lengths of three semi-principal axes, and (x', y', z') are the surface coordinates of the spheroid in the body-fixed system. For an oblate spheroid, a = b > c. In this study, the equivalent spherical radius of the spheroid is defined as the radius of a sphere of the same volume as the oblate spheroid,

$$R = (abc)^{1/3} \tag{2}$$

As shown in Fig. 1, an oblate spheroid is placed symmetrically on the central plane of an incompressible flow confined by two parallel planes moving in opposite directions with speed  $U_0$ . The distance between the two plates is 2H, and the length and width of the planes are 2L and 2W, respectively. The background flow shear rate (G) is adjusted by  $U_0$  and H. The minor axis of the oblate spheroid is parallel to the vorticity vector of the flow, and the particle is allowed to rotate in response to surface pressure and shear stress

exerted by the surrounding fluid. The density of the particle is the same as that of the fluid. The outflow condition is applied at the streamwise and spanwise boundaries. The undisturbed shear rate of the simple shear flow is defined as:

$$G = \frac{U_0}{H} \tag{3}$$

For oblate spheroids of different aspect ratios, the Reynolds number is defined uniformly based on the equivalent spherical radius R and the background flow shear rate G,

$$Re = \frac{GR^2}{V} \tag{4}$$

where  $\nu$  is the kinematic viscosity of the carrier fluid.

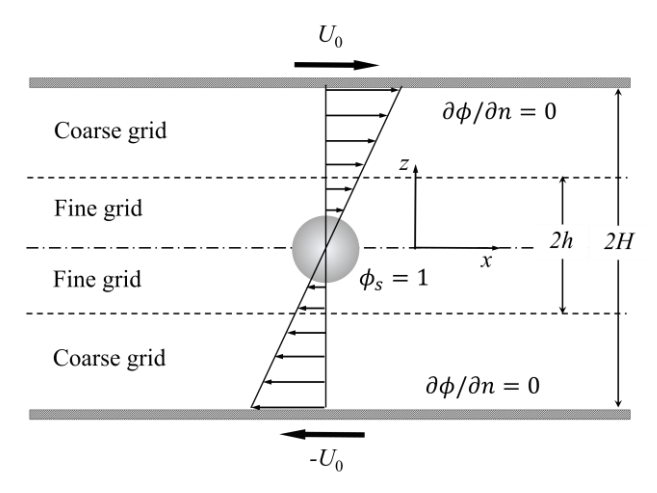


Fig. 1. Physical model of an oblate spheroid suspended in a simple shear flow with passive scalar released from particle surface. Zero scalar flux condition is applied on the top and bottom planes as well as the lateral domain boundaries. The minor axis is parallel to the vorticity vector of the background flow. A fine grid of vertical dimension *2h* is used in the middle region to resolve the detailed fluid and particle dynamics and transport of passive scalar.

To predict heat and mass transport, temperature and mass concentration are modeled as the concentration ( $\phi$ ) of a passive scalar released at particle surface, where  $\phi$  is fixed at  $\phi_s=1$ . The Peclet number, which characterizes the effect of flow shear on scalar transport, is defined as

$$Pe = \frac{GR^2}{D} = ReSc \tag{5}$$

where Sc = v/D is the Schmidt number of the passive scalar in the fluid and D is the mass diffusivity. To compare the scalar release rate of oblate spheroids of different aspect ratios, it is convenient to use the nondimensional release rate, i.e. the Sherwood number (Sh), which is defined based on the radius and surface area of the sphere of the same volume,

$$Sh = \frac{QR}{DA\phi_S} \tag{6}$$

where Q is the release rate of the passive scalar from the particle surface,  $A = 4\pi R^2$  the surface area of the sphere, and  $\phi_s = 1$  the concentration of passive scalar at particle surface.

A complete description of the problem includes the Reynolds number (Re), Schmidt number (Sc), particle aspect ratio ( $\Lambda = a/c$ ), and the ratios of the height (2H), width (2W), and length (2L) of the computational domain to the radius of sphere of the same volume (2H/R, 2W/R, and 2L/R). The diffusion-controlled transport process was addressed by Wang et al.<sup>7</sup>, so the focus of this study is the advective enhancement of heat and mass transport. Following the parameters of realistic applications, such as drug dissolution, the Reynolds number range is  $O(10^{-3})$  to O(1). Considering grid resolution required for the simulation of transport process of large Sh, the Schmidt number is limited to the range from  $O(10^{1})$  to  $O(10^{2})$ . To minimize the influence of boundaries, the height, width, and length of the computational domain are over an order of magnitude larger than the radius of the sphere.

Here we only consider the transport process in the stable state, in which the oblate spheroid spins with a constant speed about its minor axis. The minor axis of the spheroid is initially parallel to the vorticity vector of the background shear flow, and then the spheroid moves freely, driven by the surround fluid. After an initial evolving period, the fluid and particle motion as well as the scalar transport enter a steady state. When the scalar release rate is sufficiently close to a constant value, the analysis is conducted.

## 3. Numerical Methods

We developed a 3D numerical method based on a multigrid strategy within the lattice Boltzmann (LB) framework. The LB method is highly parallelizable and highly capable in dealing with stationary and moving solid boundaries with complex geometries. The dependent variable is the particle distribution function  $\mathbf{f}(\mathbf{x},t)$ , which quantifies the probability of finding an ensemble of molecules at position  $\mathbf{x}$  with velocity  $\mathbf{e}$  at time  $t^{31-33}$ . Continuum-level velocity  $\mathbf{u}(\mathbf{x},t)$  and density  $\rho(\mathbf{x},t)$  are obtained from moments of  $\mathbf{f}(\mathbf{x},t)$  over velocity space. In three dimensions, the velocity vector  $\mathbf{e}$  can be discretized into 15, 19, or 27 components in what are referred to as the D3Q15, D3Q19 and D3Q27 approaches<sup>31</sup>. Here we apply the D3Q19 approach, largely to minimize computational load, with the recognition that the flow Reynolds number is relatively low.

The LB equation with the Bhatnagar-Gross-Krook<sup>34</sup> representation for the collision operator<sup>32</sup> is written as,

$$\mathbf{f}(\mathbf{x} + \mathbf{e}\delta_t, t + \delta_t) - \mathbf{f}(\mathbf{x}, t) = -\frac{1}{\tau} (\mathbf{f}(\mathbf{x}, t) - \mathbf{f}^{eq}(\mathbf{x}, t))$$
(7)

where the discretized velocity vector **e** for D3Q19 is,

$$\mathbf{e}_{\alpha} = \begin{cases} (0,0,0) & \alpha = 0\\ (\pm 1,0,0), (0,\pm 1,0), (0,0,\pm 1) & \alpha = 1,2,\cdots,6\\ (\pm 1,\pm 1,0), (\pm 1,0,\pm 1), (0,\pm 1,\pm 1) & \alpha = 7,8,\cdots,18 \end{cases}$$
(8)

where  $\alpha$  is the index of components of velocity vector  $\mathbf{e}$ . The left-hand side (LHS) of Eqn. (7) describes "streaming," the exchange of momentum between neighboring lattice nodes as a result of bulk advection and molecular diffusion. The right-hand side (RHS) describes the mixing, or collision of molecules that drive the distribution function ( $\mathbf{f}(\mathbf{x},\mathbf{t})$ ) toward the equilibrium distribution function ( $\mathbf{f}^{eq}(\mathbf{x},\mathbf{t})$ ), with a relaxation time scale,  $\tau$ . The relaxation time is linearly related to the fluid kinematic viscosity  $\nu$  by

$$v = (2\tau - 1)c\delta x/6 \tag{9}$$

where  $\delta x$  is the lattice spacing and  $c = \delta x/\delta t$  is the basic speed on the lattice. In the low Mach number limit, the equilibrium distribution for the D3O19 model is<sup>31</sup>

$$\mathbf{f}^{eq}(\mathbf{x},t) = w_{\alpha}\rho(\mathbf{x},t) \left[ 1 + 3\frac{\mathbf{e}_{\alpha} \cdot \mathbf{u}}{c^2} + \frac{9}{2}\frac{(\mathbf{e}_{\alpha} \cdot \mathbf{u})^2}{c^4} - \frac{3}{2}\frac{\mathbf{u} \cdot \mathbf{u}}{c^2} \right]$$
(10)

where  $w_{\alpha}$  are weighting factors,  $w_0 = 1/3$ ,  $w_{\alpha} = 1/18$  for  $\alpha = 1 - 6$ , and  $w_{\alpha} = 1/36$  for  $\alpha = 7 - 18$ . The continuum-level fluid density  $\rho(\mathbf{x}, t)$  and momentum  $\rho \mathbf{u}(\mathbf{x}, t)$  are obtained from the discretized moments of the particle distribution function,

$$\rho(\mathbf{x},t) = \sum_{\alpha} f_{\alpha}(\mathbf{x},t), \quad \rho(\mathbf{x},t)\mathbf{u}(\mathbf{x},t) = \sum_{\alpha} f_{\alpha}(\mathbf{x},t)\mathbf{e}_{\alpha}$$
(11)

In the treatment of moving particle surfaces, we used the 2<sup>nd</sup> order accurate scheme of Lallemand and Luo<sup>35</sup>. This method is based on the simple bounce-back boundary scheme and interpolations. If the distance fraction of the first fluid node from the solid boundary is less than half of one lattice space, the computational quantities are interpolated before propagation and bounce-back collision. If the distance fraction is greater than a half lattice space, interpolation is performed after propagation and bounce-back collision. The momentum exerted by the moving boundary is given by these terms, which were developed by Ladd<sup>36</sup> and Bouzidi et al.<sup>37</sup>

The motion of the particle is obtained by solving Newton's equations of motion,

$$M d\mathbf{U}(t)/dt = \mathbf{F}(t) \tag{12}$$

$$\mathbf{I} \cdot d\mathbf{\Omega}(t)/dt + \mathbf{\Omega}(t) \times [\mathbf{I} \cdot \mathbf{\Omega}(t)] = \mathbf{T}(t)$$
(13)

where M is the mass of a solid particle,  $\mathbf{I}$  the inertial tensor,  $\mathbf{U}$  the translational velocity,  $\mathbf{\Omega}$  is the angular velocity, and  $\mathbf{F}$  and  $\mathbf{T}$  are the total force and torque on the particle, respectively. At each fluid boundary node  $\mathbf{x}_b$ , the force is calculated by the exchange of distribution function between the fluid and solid.

$$\mathbf{F}_{b}(\mathbf{x}_{b},t) = -\sum_{\alpha} \left[ f_{\overline{\alpha}}(\mathbf{x}_{b},t+\delta_{t}) - \hat{f}_{\alpha}(\mathbf{x}_{b},t_{+}) \right]$$
(14)

where  $f_{\overline{\alpha}}$  is the distribution transferred from the solid boundary, including the additional momentum due to boundary motion,  $\hat{f}_{\alpha}$  is the post-collision distribution transferred from the flow to the boundary. According to Aidun et al.<sup>38</sup>, the total force includes three components, the force due to the communication of distribution function  $(\mathbf{F}_b(\mathbf{x}_b,t))$ , the force due to momentum transfer from fluid to solid when some grid

nodes are covered by solid ( $\mathbf{F}_c(\mathbf{x},t)$ ), and the force due to momentum transfer from solid to fluid when some grid nodes are uncovered by solid ( $\mathbf{F}_u(\mathbf{x},t)$ ). The latter two are given as,

$$\mathbf{F}_{c}(\mathbf{x}_{c},t) = -\sum_{\alpha} [f_{\alpha}(\mathbf{x}_{c},t)\mathbf{e}_{\alpha}]$$
(15)

$$\mathbf{F}_{u}(\mathbf{x}_{u},t) = -\rho(\mathbf{x}_{u},t)\mathbf{u}(\mathbf{x}_{u},t) \tag{16}$$

The total force and torque are calculated by summing the force and torque at each fluid boundary node and each covered and uncovered fluid node,

$$\mathbf{F}(t) = \sum_{FBN} \mathbf{F}_b(\mathbf{x}_b, t) + \sum_{CN} \mathbf{F}_c(\mathbf{x}_c, t) + \sum_{UN} \mathbf{F}_u(\mathbf{x}_u, t)$$
(17)

$$\mathbf{T}(t) = \sum_{FRN} (\mathbf{x}_h - \mathbf{X}_o) \times \mathbf{F}_h(\mathbf{x}_h, t)$$
 (18)

where FBN, CN, and UN denote the fluid boundary nodes, covered, and uncovered nodes.  $X_o$  is the central coordinate of the solid particle.

To solve the process of heat and mass transport, the passive scalar is distributed in the flow field. The moment propagation method developed by Frenkel and Ernst<sup>39</sup>, Lowe and Frenkel<sup>40</sup>, and Merks et al.<sup>41</sup> is used to solve the scalar. In this method, a scalar quantity is released in the lattice and a scalar concentration field variable is propagated at the continuum level for each scalar using the distribution function. Let  $\phi(\mathbf{x}, t)$  be the continuum-level scalar concentration on the lattice at location  $\mathbf{x}$  at time t, the advancement of the scalar concentration at the next step is given by

$$\phi(\mathbf{x}, t + \delta t) = \sum_{\alpha} P_{\alpha}(\mathbf{x} - \mathbf{e}_{\alpha} \delta t, t + \delta t) + \phi(\mathbf{x}, t) \Delta^{*}$$
(19)

$$P_{\alpha}(\mathbf{x} - \mathbf{e}_{\alpha}\delta t, t + \delta t) = \left[\frac{\hat{f}_{\alpha}(\mathbf{x} - \mathbf{e}_{\alpha}\delta t, t_{+})}{\rho(\mathbf{x} - \mathbf{e}_{\alpha}\delta t, t)} - w_{\alpha}\Delta^{*}\right]\phi(\mathbf{x} - \mathbf{e}_{\alpha}\delta t, t)$$
(20)

where  $\hat{f}_{\alpha}$  denotes the post-collision pre-streamed distribution function in  $\alpha$ -direction,  $t_+$  implies a time after collision but before streaming, and  $\Delta^*$  is the fraction of  $\phi(\mathbf{x}, t)$  that remains on the lattice node during the time advancement.  $\Delta^*$  is related to the molecular diffusivity of the passive scalar as,

$$\Delta^* = 1 - 6D/c\delta x \tag{21}$$

One advantage of the moment propagation method is that the upper bound of Peclet number is much larger than in other methods, and so the calculation is more stable.

To reduce the computational load imposed by the exceptionally fine full-domain uniform grid required by the LB method to appropriately resolve a spheroidal particle, a dual-lattice method developed by Filippova and Hanel<sup>42</sup> and Yu et al.<sup>43</sup> was used. With this approach a fine grid is placed in a subregion surrounding the particle, as shown in Fig. 1, and a coarse grid is used in the other subregions. To maintain continuity of viscosity across the interface, the relaxation time between the fine and coarse grids must therefore satisfy,

$$\tau_f = \frac{1}{2} + m \left( \tau_c - \frac{1}{2} \right) \tag{22}$$

where  $m = \delta x_c / \delta x_f$  is the ratio of the lattice spacing between the two grid systems, and the subscripts c and f indicate the coarse and fine grids, respectively. In the simulations m = 5 is used in all cases.

To maintain continuity of density and momentum across the interface of fine and coarse grids, the equilibrium distribution function of the neighboring grid system must be the same at the interface,

$$\mathbf{f}^{eq,c} = \mathbf{f}^{eq,f} \tag{23}$$

To maintain continuity of viscous deviatoric stress at the interface, the transfer of the post-collision distribution functions between the two grids is given by

$$\hat{\mathbf{f}}^c = \hat{\mathbf{f}}^{eq,f} + m \frac{\tau_c - 1}{\tau_f - 1} (\hat{\mathbf{f}}^f - \mathbf{f}^{eq,f})$$
(24)

$$\hat{\mathbf{f}}^f = \hat{\mathbf{f}}^{eq,c} + \frac{\tau_f - 1}{m(\tau_c - 1)} (\hat{\mathbf{f}}^c - \mathbf{f}^{eq,c})$$
(25)

where  $\hat{\mathbf{f}}$  is the post-collision distribution function. The multigrid strategy is also implemented in the momentum propagation method. The details of this method can be found in Wang et al.<sup>33</sup> In the simulation, the height of the subregion of fine grid, denoted by 2h, is 8 times the radius of a sphere of the volume of the oblate spheroid.

In moment propagation method, the continuity of diffusion coefficient across the interface of fine and coarse grids gives,

$$\Delta_f^* = 1 - m(1 - \Delta_c^*) \tag{26}$$

At the interface, the scalar concentration is continuous,

$$\phi_c = \phi_f \tag{27}$$

At the boundary of each grid, there is an overlap between the fine and coarse grids with the boundary of each grid located in the interior of the other. The scalar concentration is obtained from the other grid, either directly or by interpolation. All nodes not on the boundaries are calculated with the moment propagation method in the usual way.

## 4. Result Validation

To examine the grid sensitivity of the results, we conducted the simulations of fluid flow and scalar transport around an oblate spheroid with a = 1.5R, for Re = 1 and Sc = 100. Two different sets of grids, with 30 and 40 fine grid points over one major radius, corresponding to 20 and 27 fine grid points over one equivalent spherical radius, were used. Figure 2 shows the profiles of streamwise velocity  $(u_x)$  and

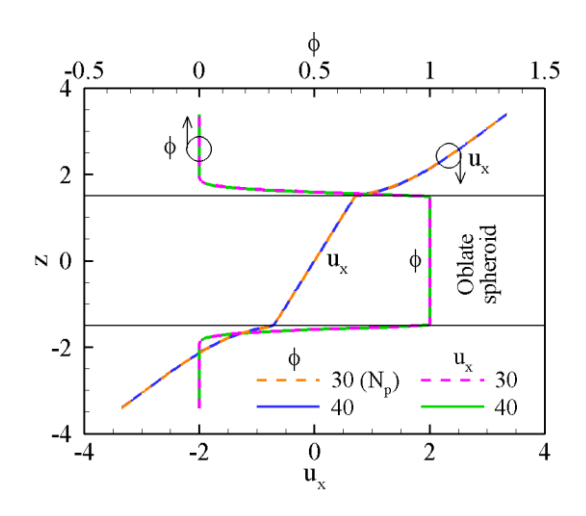


Fig. 2. Effect of grid resolution on streamwise velocity  $(u_x)$  and concentration of passive scalar  $(\phi)$  along the vertical central line of an oblate spheroid with a=1.5R, for Re=1 and Sc=100. The relative deviation is less than 0.3%.  $N_p$  is the number of grid points over one major radius.

concentration of passive scalar ( $\phi$ ) along the vertical line through particle center. Excellent convergence between the two sets of grids was obtained, with maximum deviation of the quantities of less than 0.3%. Therefore, the coarser grid system corresponding to 20 grid points over one equivalent spherical radius was used in the simulations. Section 5 presents a detailed discussion of the results.

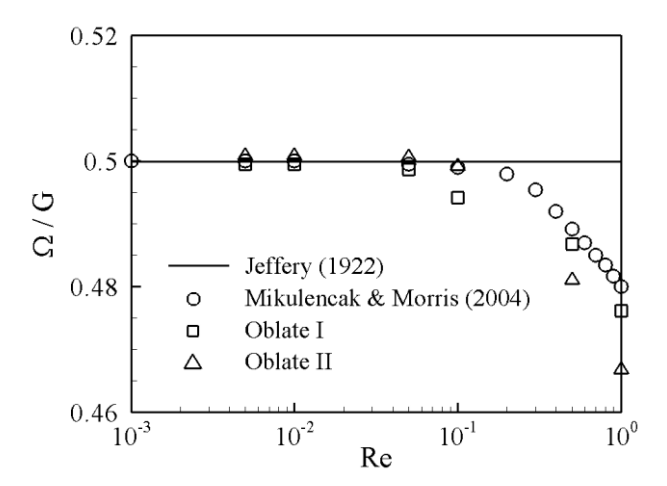


Fig. 3. Dependence of angular velocity of oblate spheroids on Reynolds number. Oblate I: a = 1.5R, and Oblate II: a = 2R. Data of Mikulencak and Morris<sup>44</sup> (2004) are for circular cylinder, and data of Jeffery's theory<sup>20</sup> are for oblate spheroids at Re = 0.

In order to validate the numerical results, we compare our results with those available in the literature as discussed above. According to Jeffery<sup>20</sup>, when an oblate spheroid spins about its minor axis, which is parallel to the vorticity vector, the angular velocity is  $\Omega=0.5G$  when Re=0. In Fig. 3, We compare the normalized angular velocities  $(\Omega/G)$  of the oblate spheroids with  $\alpha=1.5R$  and 2R for  $0.005 \le Re \le 1$  with the prediction of Jeffery's theory<sup>20</sup> for oblate spheroids at Re=0 and the data of Mikulencak and Morris<sup>44</sup> for circular cylinder. When Re<0.1, the numerical results agree well with Jeffery's theory, with relative error less than 0.1%. When Re>0.1, the effects of Reynolds number and particle aspect ratio appear. As Re increases,  $\Omega/G$  decreases for both spheroids. This trend is consistent with the data of Mikulencak and Morrris<sup>44</sup> for circular cylinder. In addition, larger aspect ratio  $(\Lambda = \alpha/c)$  leads to larger deviation from Jeffery's prediction. For heat and mass transport, no data have been found for oblate spheroids in the literature, so we use the result of a spherical particle, which is a special case of oblate

spheroids, for the validation. In Fig. 4 we compare the normalized scalar release rate, i.e., Sherwood number (Sh), of a spherical particle for Re close to zero with the predictions of the asymptotic theories of Frankel and Acrivos<sup>10</sup>, Batchelor<sup>12</sup>, and Polyanin and Dil'man<sup>13</sup> for Re = 0. As shown in the figure, three asymptotic theories do not give very close results. Overall, the numerical results compare well with the three theories. The deviation decreases apparently as Re decreases from 0.01 to 0.001. This comparison validates the accuracy of the results to a certain extent. It also shows that the boundary effect is negligible when dealing with small Reynolds numbers.

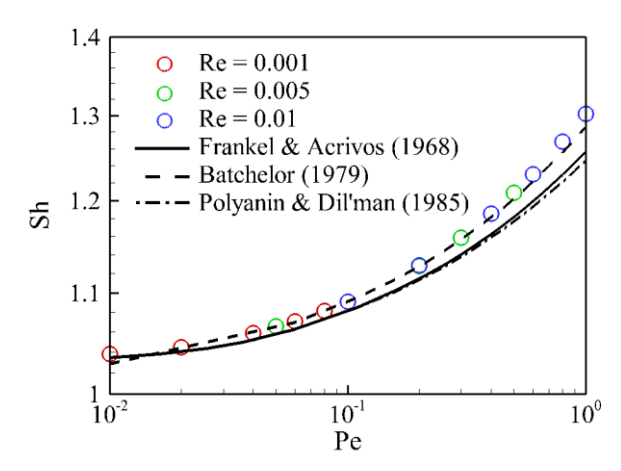


Fig. 4. Normalized scalar release rate characterized by Sherwood number (Sh) versus Peclet number (Pe). Symbols: numerical simulation for Re close to zero, lines: the asymptotic theories of Frankel and Acrivos<sup>10</sup>, Batchelor<sup>12</sup>, and Polyanin and Dil'man<sup>13</sup> for Re = 0.

## 5. Results And Discussion

In this section, the fluid and particle dynamics and the transport characteristics of passive scalar in a system of a single oblate spheroid of various aspect ratios are analyzed. Table 1 summarizes the cases considered in terms of particle radii, Reynolds, and Schmidt numbers. The ratios of the length (x direction), width (y direction), and height (z direction) of the computational domain to the radius of a sphere of the same volume as our oblate spheroid are fixed at 2L/R = 100, 2W/R = 20, and 2H/R = 20, respectively. The ratio of the height of the subregion of fine grid to the radius of sphere is 2h/R = 8. The width and

length are the same as that of the computational domain. The ratio of the lattice spacing between the two grid systems is fixed at m = 5.

Table 1. Cases of different particle radii, Reynolds, and Schmidt numbers.

a/R(=b/R)	c/R	Re	Sc
1.5	1 / 1.52	0.005, 0.01, 0.05, 0.1, 0.5, 1	20, 40, 60, 80, 100
2	1 / 2 <sup>2</sup>	0.005, 0.01, 0.05, 0.1, 0.5, 1	20, 40, 60, 80, 100
1.25, 1.75, 2.5	1/1.25 <sup>2</sup> , 1/1.75 <sup>2</sup> , 1/2.5 <sup>2</sup>	0.1	20, 40, 60, 80, 100

At the beginning, the motion of the surrounding fluid is set as an undisturbed simple shear flow, and the angular velocity of the oblate spheroid is made equal to 0.5G. The concentration of passive scalar in the fluid is zero everywhere. After an initial evolving period, the fluid and particle motion as well as the scalar transport enter a steady state. Then the analysis is conducted. The steady state is considered to be reached

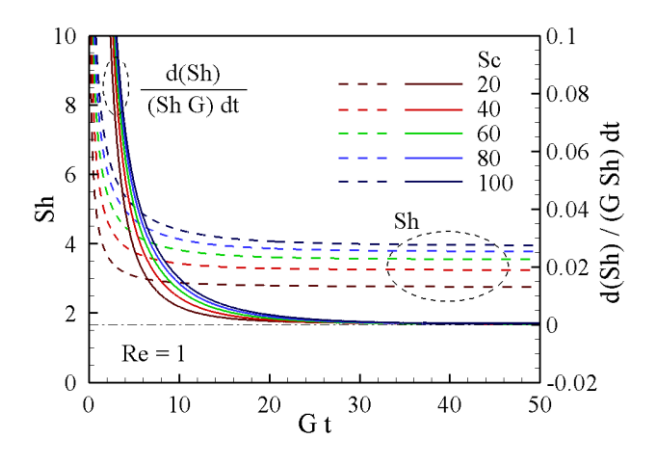


Fig. 5. Variations of Sh and d(Sh)/(Sh G dt) with normalized time, Gt, of an oblate spheroid with a = 1.5R for Re = 1.

when the normalized Sh change rate, d(Sh)/(Sh G dt), becomes less than  $10^{-3}$ . Figure 5 shows the variations of Sh and d(Sh)/(Sh G dt) with normalized time, Gt, of an oblate spheroid with a = 1.5R for Re = 1. Five Sc are considered. As shown in the figure, all Sh asymptotically approach constant values over time, and d(Sh)/(Sh G dt) approach zero. The cases with smaller Sc converge faster.

Here we use the case of a = 1.5R and Re = 1 as an example to demonstrate the basic flow structure and scalar transport characteristics. Figure 6 shows the typical streamlines around the spheroid. In the steady state, the streamlines coincide with the trajectories of the fluid particles, so the streamlines depict the transport of passive scalar through flow advection. As shown in the figure, the flow structure is composed of several different patterns of streamlines. First, on the lateral sides, the rotating spheroid drives the fluid near its surface to rotate with it. The unbalanced centrifugal force pushes the rotating fluid to a larger radial direction, forming an outward spiral flow (increasing radial coordinate; red lines) along the spheroid surface. This flow originates somewhere near the minor axis and approaches the spheroid, forming a region of spiral

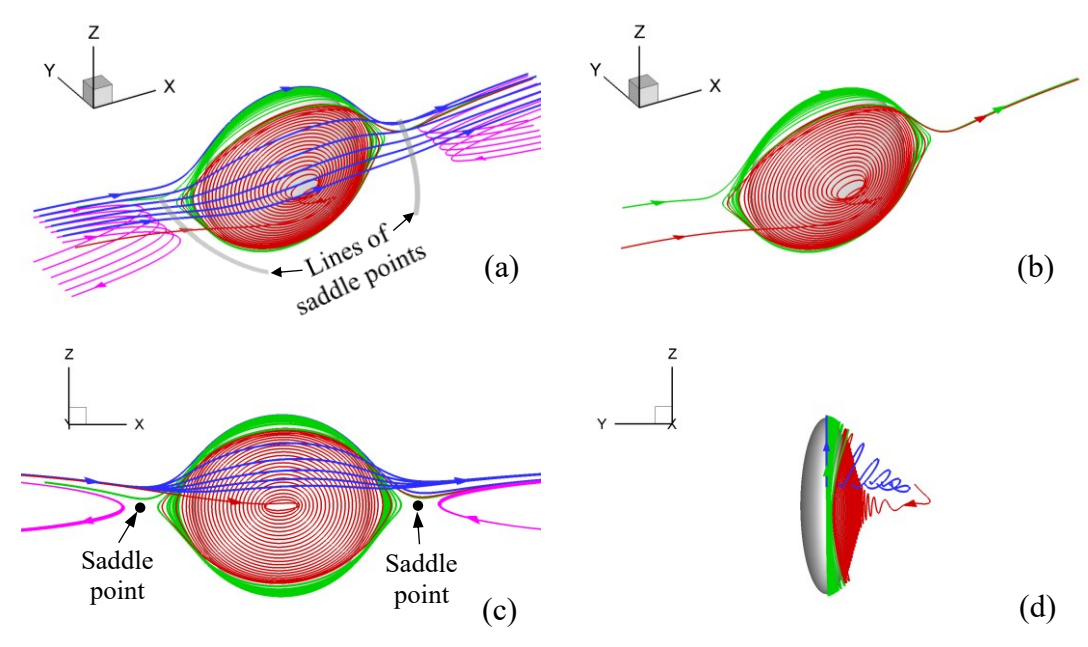


Fig. 6. Typical 3D streamlines around an oblate spheroid of a = 1.5R for Re = 1. (a, b) Perspective view, (c) side view, and (d) front view. Red: outward (increasing radial coordinate) spiral flow originating from a point transverse to the x-z plane, green: inward (decreasing radial coordinate) spiral flow originating from a point on the central x-z plane, purple: recirculating wake flow originating far upstream, blue: outer bypassing flow wrapping the spiral and reversal flows. The outer flow (blue) shifts laterally when passing by the spheroid, driving the inward spiral flow (green). The outward (red) and inward (green) spiral flows converge on a closed line on the spheroid surface and travels downstream together.

flows on the lateral sides. This spiral flow region is essentially a variation of the Stewartson layer on a rotating flat plate, which has been extensively investigated<sup>45-47</sup>. The major difference between the spiral flow layer in this study and Stewartson layer is that this spiral flow layer appears on a spheroidal surface and interacts with the outer simple shear flow. Second, near the equator of the spheroid where  $y \approx 0$ , the rotating spheroid drives a thin layer of flow on its surface, in which the fluid recirculates with the spheroid (green lines). Third, outside this flow layer, the fluid passes the spheroid and flows downstream directly (blue lines). The outer passing fluid tends to choose a shorter path, so it shifts laterally to the lateral sides as shown in Fig. 6(d). The lateral shift of the outer flow (blue lines) causes the fluid in the flow layer (green lines) near the equator to laterally shift along the spheroid surface, forming an inward (decreasing radial coordinate) spiral flow. At a certain place on the side surface, the inward flow meets the outward flow originating from the lateral area, and they merge, leaving the surface and finally travelling downstream. The inward spiral flow originates upstream of the spheroid on the central x-z plane, and leaves the spheroid somewhere away from the central x-z plane. Fourth, on either side of the oblate spheroid along the flow axis, there is a recirculating wake, in which the fluid approaches the spheroid near the axis and turns back before touching the spheroid (purple lines). The recirculating wakes are separated from the spiral flows surrounding the spheroid by two lines of saddle points (Figs. 6(a, c)). The spiral flows and the recirculating wakes are wrapped by the outer passing flow, which drives the rotation of spheroid and triggers the spiral flows and recirculating wakes. Essentially, the flow structure around an oblate spheroid is similar to that around a sphere, which has been extensively analyzed<sup>14, 15, 44</sup>. The behaviors of the flow components and the interactions among them work as an ensemble to form a complex mechanism for the transport of passive scalar.

Under the action of the surrounding flows, scalar transport exhibits a different pattern from that of diffusion transport. Figure 7 shows the pattern of scalar concentration ( $\phi$ ) around an oblate spheroid of a = 1.5R for Re = 1 and Sc = 100. The particle geometry and Reynolds number are the same as that in Fig. 6. On the windward (upper left and lower right) sides of the spheroid, the impact of the outer flow significantly

decreases the thickness of scalar boundary layer, through which  $\phi$  changes from 1 at spheroid surface to 0 in the ambient fluid. On the leeward (upper right and lower left) sides, the passive scalar released at the spheroid surface is carried by the passing flow and advected downstream. On the lateral sides, the passive scalar is transported laterally from the spheroid surface to the ambient fluid through a scalar boundary layer

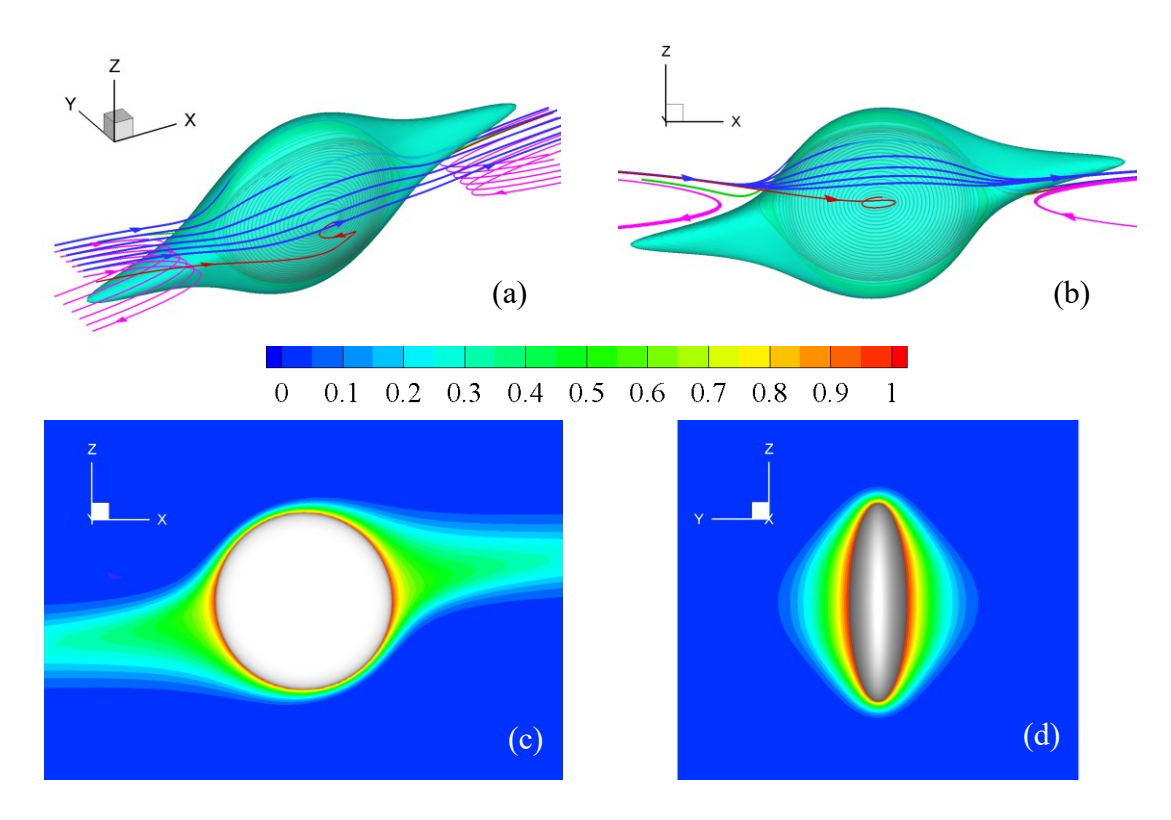


Fig. 7. Patterns of scalar concentration ( $\phi$ ) around an oblate spheroid of a=1.5R for Re=1 and Sc=100. (a) and (b) show the 3D iso-surfaces of  $\phi=0.3$  together with the typical streamlines; (c) and (d) show the iso-contours of  $\phi$  on the central x-z and y-z planes.

that is thicker than that on the windward sides. Compared with pure diffusion, the pattern shown in this figure is the outcome of a more complex transport mechanism.

To identify the mechanism of scalar transport from the spheroid surface to the ambient fluid, we plot the contours of scalar concentration ( $\phi$ ) on the *x-z* and *y-z* planes, together with the 3D streamlines, in Figs. 8(a) and (b). It is seen in Fig. 6 that the spheroid is surrounded by a flow layer consisting of an outward spiral flow on the lateral sides and an inward spiral flow near the equator. The passive scalar released at spheroid surface, therefore, is first transferred to the surrounding spiral flows through pure diffusion. In the limit case of  $Sc = \infty$ , where the molecular diffusivity D = 0, the released passive scalar will be transported

by the surrounding spiral flows away from the spheroid surface through pure advection. The spiral streamlines depict the path of scalar transport. In the case of finite Schmidt number (Sc), molecular diffusion provides important scalar transport across the streamlines. As shown in Figs. 8(a) and (b), the outer passing flow hits the windward sides (upper left and lower right sides) of the spheroid and then travels downstream along the top and bottom surfaces as well as the lateral sides of the spheroid. During this process, the passing flow gains passive scalar from the spiral flows surround the spheroid via molecular diffusion across the streamlines. As a result, the scalar concentration ( $\phi$ ) of the passing flow increases gradually. Since the spiral flows only exist in the thin layer on spheroid surface, the spiral flows lose most of their passive scalar to the passing flow after leaving the spheroid, and outer passing flow transports most

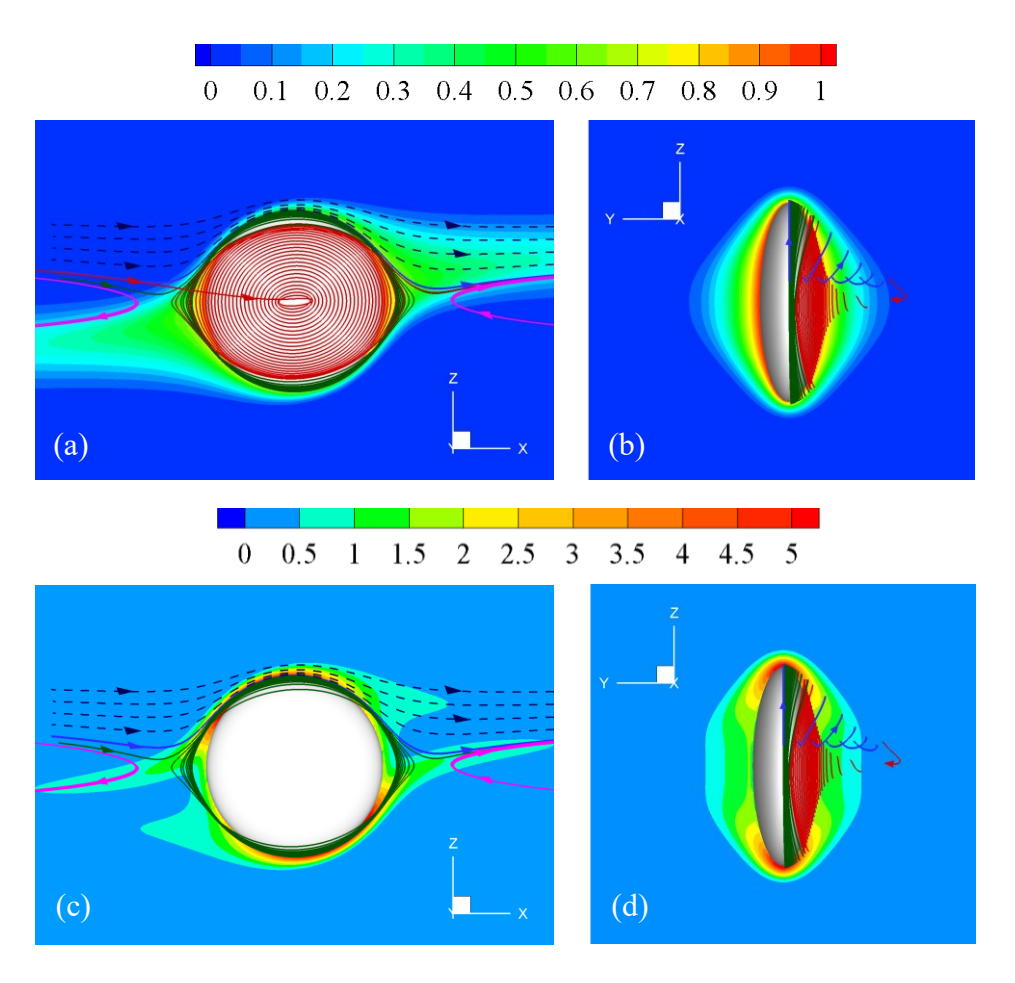


Fig. 8. Transport mechanism of passive scalar illustrated by the patterns of scalar concentration  $(\phi)$  and magnitude of the gradient of scalar concentration ( $\|\nabla\phi\|$ ). (a) and (b) show the iso-contours of  $\phi$  on the central x-z and y-z planes, together with the 3D streamlines surrounding the spheroid; (c) and (d) show the iso-contours of  $\|\nabla\phi\|$  on the central x-z and y-z planes.

of the passive scalar downstream via flow advection. It is seen from the streamline patterns in Fig. 6 that there is a thick flow layer with an outward spiral flow on the lateral side of the spheroid. Since the flow spirals towards the spheroid in this layer, the released passive scalar has to be transported against the streamlines by molecular diffusion through this layer to the outer passing flow, and then can be transported downstream by the outer flow.

To accentuate the diffusion process, we plot the modulus of the gradient of scalar concentration ( $\|\nabla\phi\|$ ) on the *x-z* and *y-z* planes together with the 3D streamlines in Figs. 8(c) and (d). It can be seen that the molecular diffusion mainly occurs in four regions. The first is in the flow layer on the windward spheroid surface, where passive scalar is transported from spheroid surface to the spiral flows, and then to the outer passing flow. The second is downstream of the leeward side, where passive scalar is transported from the outer flow just past the spheroid surface to the flow further outside. The third is in the wake flow near the flow axis (z=0), where the passive scalar is transported from the passing flow to the downstream part of the spiral flows, and then to the recirculating wake flow near the axis. The recirculating wake flows also help transport passive scalar downstream. The fourth region is the layer of spiral flows on the lateral sides of the spheroid, where the passive scalar is transported from the spheroid surface to the spiral flows, and then to the outer passing flow. During the process, the spiral flows on the spheroid surface, the recirculating wake flows on the axis, and the outer passing flow together form a coupled transport mechanism for the passive scalar, involving both molecular diffusion and flow advection.

According to the coupled transport mechanism, the passive scalar is transported through the fluid layer of spiral flows to the outer passing flow, and then transported downstream by the outer flow through advection. The thickness of the spiral flow layer is thus an important factor in transport efficiency. In the present study, the thickness of the flow layer is determined not only by spatial coordinates, but also by Reynolds number and the aspect ratio of the oblate spheroid. Figure 9 shows the profiles of the interface between the inner spiral flows and the outer passing flow on the y-z plane through the spheroid center for different Reynolds numbers. The major radius is a = 1.5R, corresponding to an aspect ratio  $A = 1.5^3$ . The

profiles of the interface show the spatial variation of the thickness of the spiral flow layers, which extend away from the spheroid along its minor axis. The extension of the spiral flow region decreases with the increase of Re. This is because the increase of Reynolds number reduces the viscous diffusion of angular momentum of surrounding fluid in the lateral direction. The outward spiral motion of the fluid causes the flow layer thickness to decrease with the increase of radial coordinate. When the radial coordinate passes a critical value ( $r_c \approx 0.8R$ ), the trend of dependence on Reynolds number becomes opposite, and the thickness increases with the increase of Re. The reason is that the centrifugal effect is stronger at larger Reynolds number, which leads to stronger fluid motion of the outward spiral flow in the radial direction, thus increasing the thickness of the spiral flow layer.

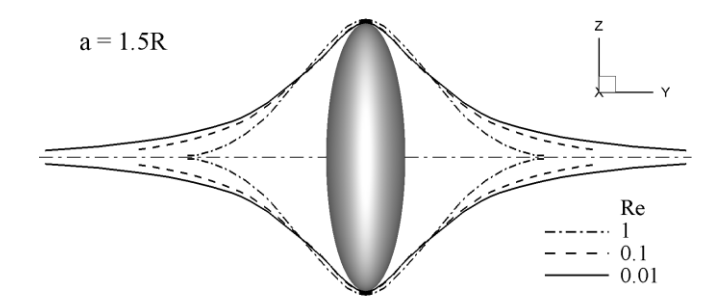


Fig. 9. Profiles of the interface between the outer bypassing flow and the inner spiral flows of an oblate spheroid of a = 1.5R.

It was shown in Wang & Brasseur<sup>9</sup> (2019) that in the range of  $Re \le O(1)$  and  $Sc \le O(10^2)$ , the transport rate of passive scalar from a sphere is primarily determined by Peclet number (Pe = ReSc). The difference in fluid velocity caused by Reynolds number has a limited effect on scalar transport. This is also the case for oblate spheroids. Although Reynolds number causes some deviation in flow velocity, it does not significantly influence the scalar transport. This can be seen from the comparison of iso-contours of scalar concentration ( $\phi$ ) between Re = 0.1 and 1 shown in Fig. 10. The Peclet number is Pe = 10, for both cases. The iso-contours of these two Reynolds numbers demonstrate similar distribution of  $\phi$  in the figure. The scalar transfer rate shown in Fig. 15 confirms this conclusion.

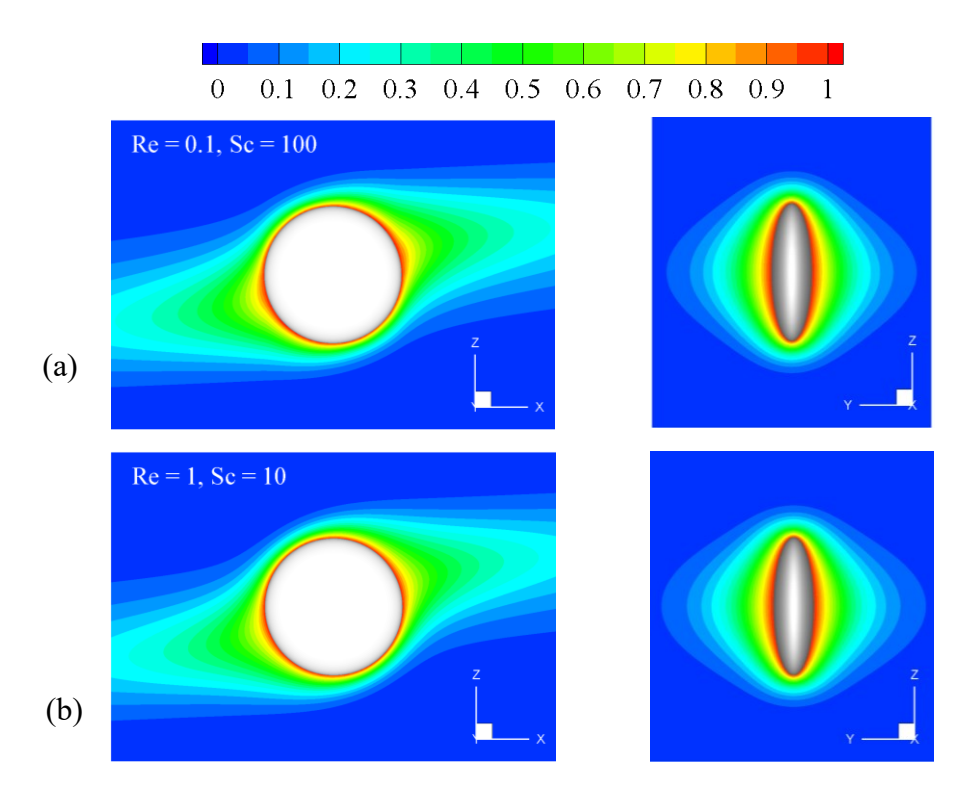


Fig. 10. Comparison of iso-contours of scalar concentration on x-z and y-z planes for Pe = 10. (a) Re = 0.1, Sc = 100, and (b) Re = 1, Sc = 10.

In addition to Reynolds number, the aspect ratio of the oblate spheroid also plays an important role in flow evolution and scalar transport. Figure 11 shows the profiles of the interface between the inner spiral flows and the outer passing flow on the y-z plane through spheroid center for different major radii. The Reynolds number is Re = 0.1. As shown in the figure, the interface profiles of spheroids of different major radii have similar shapes. A spheroid of larger major radius has a larger area of spiral flow, corresponding to a thicker flow layer. The thicker flow layer does not, however, mean that the efficiency of scalar transport is lower; in fact, although diffusive transport dominates the spiral flows on the spheroid surface, advective transport still plays a role.

It is shown in Fig. 3 that the angular velocity of the spheroid is close to 0.5*G*. The velocity difference between the rotating oblate spheroid and the ambient fluid at each vertical position can be roughly estimated as,

$$\|\mathbf{u}^r\| \approx |0.5Gz| \tag{28}$$

where z is the vertical coordinate. The oblate spheroid with a larger major radius has a larger velocity difference, leading to thinner flow and scalar boundary layer on the surface of oblate spheroid. This can be seen in the following analysis.

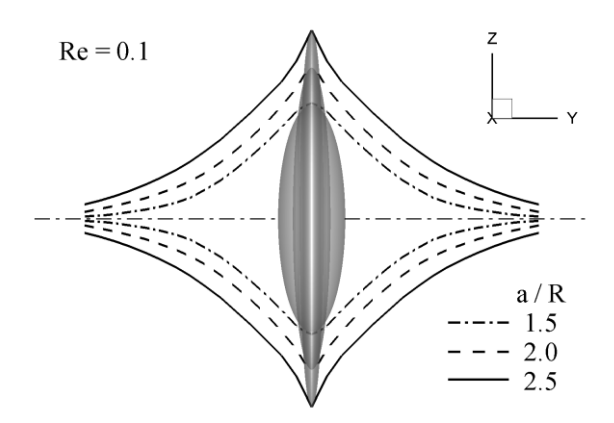


Fig. 11. Profiles of the interface between the outer bypassing flow and the inner spiral flows of oblate spheroids with different radius for Re = 0.1.

Figure 12 shows the iso-contours of the modulus of flow velocity relative to a rotating oblate spheroid with major radii a = 1.5R and 2.5R for Re = 0.1.  $\mathbf{u}^r$  is defined as,

$$\mathbf{u}^r = \mathbf{u} - \mathbf{\Omega} \times \mathbf{r} \tag{29}$$

where  $\Omega$  is the vector of angular velocity of the spheroid, and  $\mathbf{r}$  the coordinate vector in a polar coordinate system. As shown in the figure,  $\|\mathbf{u}^r\|$  changes more sharply near the spheroid surface when a=2.5R than when a=1.5R on both the x-z and y-z planes. This suggests that the boundary layer is thinner on the spheroid with larger major radii, which will lead to higher scalar transfer rate. On the x-z plane, the contour lines present an interesting square distribution near the spheroid. This is caused by the velocity field in the rotating system. Figure 13 shows the streamline patterns on the x-z plane in the frame of reference rotating with the oblate spheroids with a=1.5R and 2.5R for Re=0.1. In the range of Reynolds number considered in this study ( $Re \le 1$ ), the streamline distribution demonstrates a roughly symmetrical square pattern.

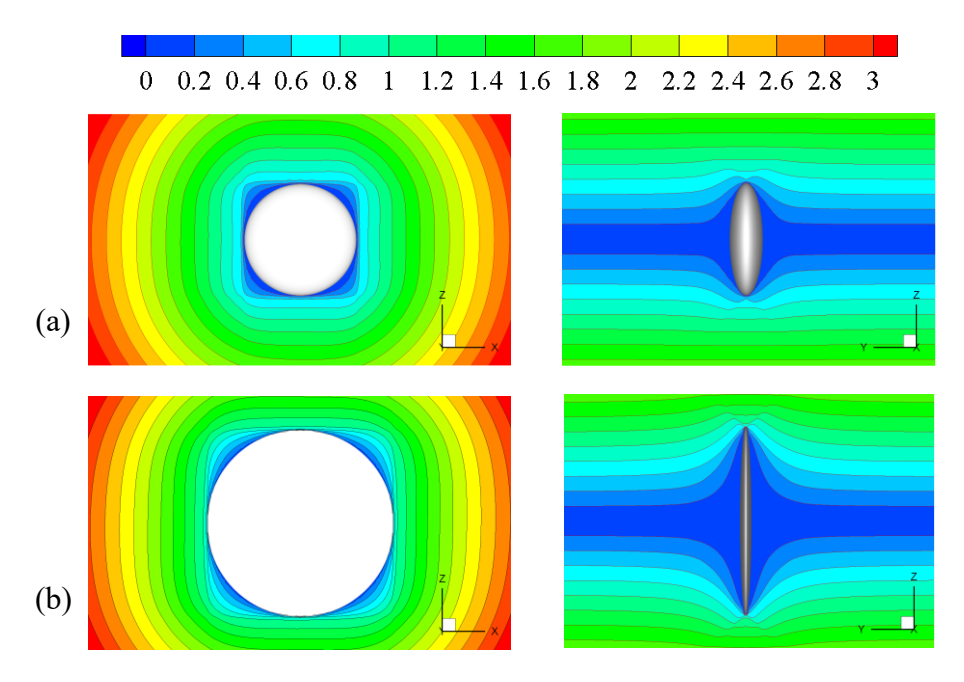


Fig. 12. Iso-contours of  $\|\mathbf{u}^r\|$  on the central x-z and y-z planes in the frame of reference rotating with the oblate spheroids with a = 1.5R and 2.5R for Re = 0.1. (a) a = 1.5R, (b) a = 2.5R. Left column: x-z plane, right column: y-z plane.

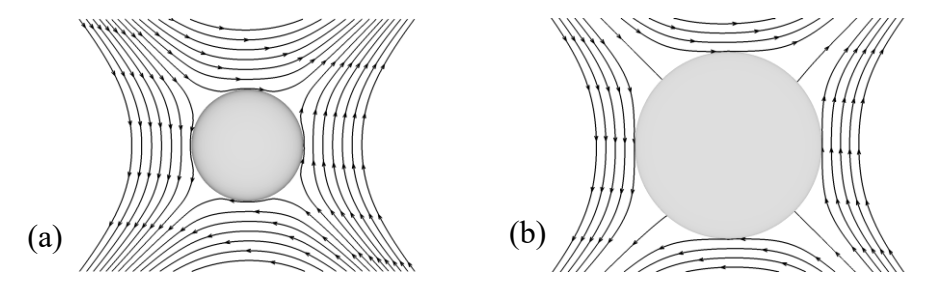


Fig. 13. Streamline patterns on the x-z plane in the frame of reference rotating with the oblate spheroids with a = 1.5R and 2.5R for Re = 0.1. (a) a = 1.5R, (b) a = 2.5R.

Figure 14 shows the patterns of scalar concentration around oblate spheroids with a = 1.5R and 2.5R for Re = 0.1 and Sc = 100. Due to the sharper variation of  $\|\mathbf{u}^r\|$  around the spheroid of a = 2.5R, as shown in Fig. 12,  $\phi$  changes more sharply near the spheroid surface, leading to an increased scalar transfer rate from the spheroid surface to the ambient fluid. In addition, the spheroid with a larger major radius has a larger surface area, which also enhances the scalar transfer rate.

The coupled transport mechanism leads to the complex dependence of scalar transport rate on the controlling parameters. In this study, we focus on the effects of Reynolds number, Schmidt number, and the aspect ratio of spheroids. In a study of mass transfer from a neutrally buoyant sphere in a simple shear

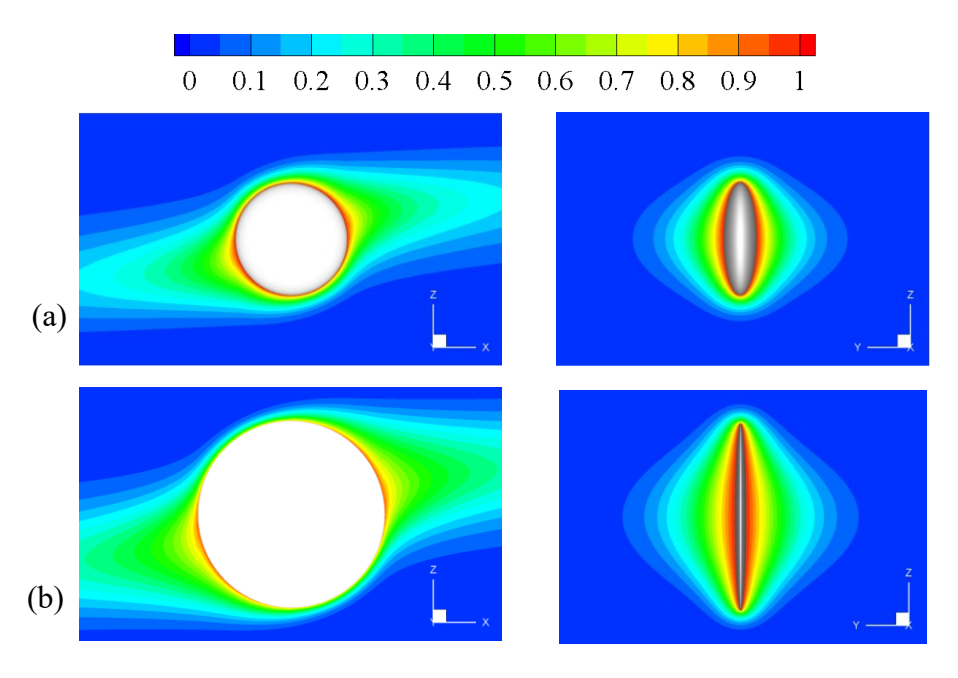


Fig. 14. Patterns of scalar concentration ( $\phi$ ) around oblate spheroids with a=1.5R and 2.5R for Re=0.1 and Sc=100. (a) a=1.5R, (b) a=2.5R. Left column: x-z plane, right column: y-z plane.

flow<sup>9</sup>, it was shown that in the range of  $Re \le O(1)$  and  $Sc \le O(10^2)$ , the nondimensionalized transfer rate, Sherwood number (Sh), is mainly determined by the Peclet number (Pe), which is defined as the product of Re and Sc. Reynolds number plays a minor role. This is also found in the results for oblate spheroids. In Fig. 15 we plot Sh against Pe in both linear and log scales for the cases simulated in this work. For the purposes of comparison, the results for a sphere are also included. For each major radius, Sh increases with increase in Pe, with Sh being more sensitive at smaller Pe. For each Pe, the increase in Re causes a slight increase in Sh. The shape of the spheroid, i.e. the major radius or the aspect ratio, has a significant effect on Sh. The increase in the major radius of the spheroid from R to 1.5R and from 1.5R to 2R leads to an overall increase in Sh. In the log scale, the curves of the oblate spheroid show patterns similar to those of the sphere, which suggests that the effect of particle shape on scalar transfer rate may be decoupled from the effects of Pe, Re and Sc. Thus, the relationship of Sh to the other parameters can be written as,

$$Sh_{oblate}(Pe, Re, a/R) = Sh_{sphere}(Pe, Re)f(a/R)$$
 (30)

where  $Sh_{oblate}$  is the Sherwood number of scalar release from an oblate spheroid,  $Sh_{sphere}$  is the Sherwood number of a sphere, and f(a/R) is a function of the major radius of the oblate spheroid. Here we use the major radius of the spheroid instead of aspect ratio as the parameter, because when the major radius is large, the flow and scalar concentration patterns as well as heat and mass transfer rate are close to that of a flat plate. Sh is more related to the major radius than the aspect ratio. In normalized form, the aspect ratio of an oblate spheroid is written as  $\Lambda = (a/R)^3$ , which is the cube of major radius. In loglog scales, the shape of the curve of Sh vs.  $\Lambda$  is the same as that of Sh vs. a/R. However, the relationship between Sh and  $\Lambda$  is indirect.

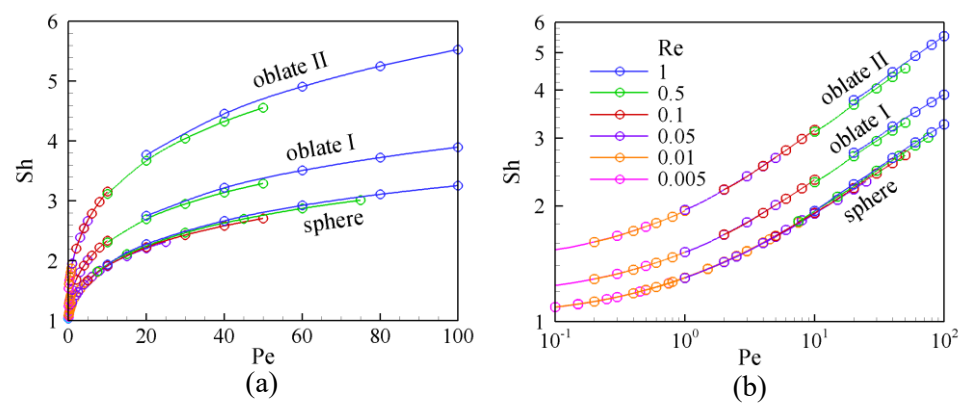


Fig. 15. Sherwood number (Sh) versus Peclet number (Pe) for oblate spheroids of different major radii. (a) linear scales, and (b) log-log scales. The symbols indicate the results of numerical simulation. Oblate I: a = 1.5R, Oblate II: a = 2.5R.

A correlation of  $Sh_{sphere}$  for a sphere in a simple shear flow as a function of Pe and Re was developed in Wang & Brasseur<sup>9</sup>. A key step to develop an analogous correlation of Sh for oblate spheroids of the form of Eqn. (30) is to find the dependence of Sh on the major radius a/R. Since function f(a/R) in Eqn. (30) is assumed to be the same for all Reynolds and Peclet numbers, we choose the data of Re = 0.1 to develop the correlation. Figure 16 shows the variation of Sh with a/R in a log-log scale. The numerical data are represented by open circles. The strong similarity of the curves for different Pe confirms the conclusion that the effect of spheroid shape can be decoupled from the other effects. As shown in the figure, Sh increases with an increase of a/R. At the same time, Sh tends to follow a linear relationship with a/R. A likely reason is that as a/R increases, the shape of the spheroid approaches a flat plate and the flow

characteristics and scalar transport around the spheroid approach the result for a flat plate, which may have some linear nature in log-log space. According to this observation, it is reasonable to assume that the relationship between  $\log(Sh_{oblate}) - \log(Sh_{sphere})$  and  $\log(a/R)$  follows a modified hyperbola equation,

$$(\log(Sh_{oblate}) - \log(Sh_{sphere}) + 1)^2 - C(\log(\alpha/R))^2 = 1$$
(31)

where C is a coefficient to be determined. Using the standard linear least squares method, the coefficient is found to be C = 2.42. Substituting Eqn. (31) into (30) gives,

$$f(a/R) = \exp(\sqrt{1 + C(\log(a/R))^2} - 1)$$
 (32)

The prediction of  $Sh_{oblate}$  of Eqn. (31) is shown in Fig. 16 as solid lines, which agrees well with the numerical data. A slight deviation can be noticed when a/R > 2. Yet the aspect ratio of the oblate spheroid corresponding to a/R = 2 is  $\Lambda = (a/R)^3 = 8$ , which is far beyond the range of usual applications. Therefore, the empirical correlation can be used with confidence in most scientific and industrial applications.

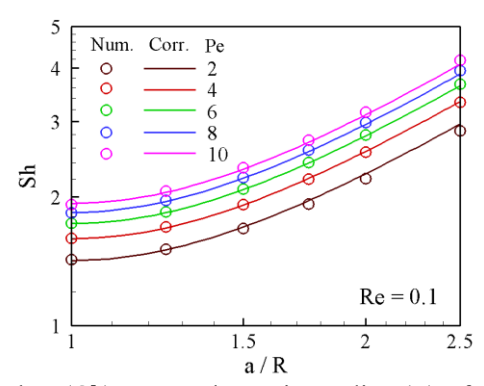


Fig. 16. Sherwood number (Sh) versus the major radius (a) of an oblate spheroid for Re = 0.1. Symbols: numerical data, lines: correlation.

## 6. Conclusion

Through high-fidelity numerical simulation based on the lattice Boltzmann method, we have conducted an in-depth study on the heat and mass transport from an oblate spheroid neutrally suspended in a simple

shear flow. In the simulation, the temperature and mass concentration are modeled as the concentration of a passive scalar released at spheroid surface. The interaction between the carrier fluid and suspended spheroid results in several flows around the spheroid, which are characterized by streamlines of different patterns. These are: outward spiral flows on the lateral side, inward spiral flows near the equator, recirculating wake flows near the flow axis, and the outer passing flow wrapping the spiral and wake flows. The passive scalar released at spheroid surface is first transported through the flow layer of the spiral flows to the outer passing flow through diffusion, and then transported downstream by the outer flow through advection. After leaving the spheroid, the outer flow passes a portion of the passive scalar to the flow further outside and the flow in the recirculating wake, which helps transport the passive scalar downstream through advection. These flow motions constitute a coupled transport mechanism for passive scalar from the oblate spheroid to the far field. The flow behaviors around the spheroid depend on both the Reynolds number of the flow and the aspect ratio of the spheroid. The changes in flow behaviors cause changes in the transport efficiency of the passive scalar. The results suggest that the effect of spheroid shape on scalar transfer rate can be decoupled from the effects of Peclet and Reynolds numbers, and this enables the development of a correlation of nondimensional scalar transfer rate, i.e. Sherwood number, for oblate spheroids, based on the well-developed correlations for a sphere.

#### **ACKNOWLEDGEMENT:**

This work was supported by the National Science Foundation (Award ID: 2138740)

## **CONFLICT OF INTEREST**

The authors have no conflicts to disclose

## **DATA AVAILABILITY**

The data that support the findings of this study are available from the corresponding author upon reasonable request.

#### References

- 1. N. Salehi, J. Al-Gousous, D. M. Mudie, G. L. Amidon, R. M. Ziff, and G. E. Amidon, "Hierarchical mass transfer analysis of drug particle dissolution, highlighting the hydrodynamics, pH, particle size, and buffer effects for the dissolution of ionizable and nonionizable drugs in a compendial dissolution vessel," Molecular Pharmaceutics 17, 3870 (2020).
- 2. J. Petersen, "Heap leaching as a key technology for recovery of values from low-grade ores—A brief overview," Hydrometallurgy **165**, 206 (2016).
- 3. K. C. Badgujar, and B. M. Bhanage, "Factors governing dissolution process of lignocellulosic biomass in ionic liquid: Current status, overview and challenges," Bioresource technology **178**, 2 (2015).
- 4. A. Chamolly, and E. Lauga, "Stochastic dynamics of dissolving active particles," The European Physical Journal E **42**, 1 (2019).
- 5. P. Costa, and J. M. S. Lobo, "Modeling and comparison of dissolution profiles," European journal of pharmaceutical sciences **13**, 123 (2001).
- 6. Y. Wang, B. Abrahamsson, L. Lindfors, and J. G. Brasseur, "Comparison and analysis of theoretical models for diffusion-controlled dissolution," Molecular Pharmaceutics 9, 1052 (2012).
- 7. Y. Wang, H. Wan, T. Wei, D. Nevares, and F. Shu, "Quasi-steady-state modelling and characterization of diffusion-controlled dissolution from monodisperse prolate and oblate spheroidal particles," Proceedings of the Royal Society A 478, 20220283 (2022).
- 8. Y. Wang, B. Abrahamsson, L. Lindfors, and J. G. Brasseur, "Analysis of Diffusion-Controlled Dissolution from Polydisperse Collections of Drug Particles with an Assessed Mathematical Model," Journal of Pharmaceutical Sciences **104**, 2998 (2015).
- 9. Y. Wang, and J. G. Brasseur, "Enhancement of mass transfer from particles by local shear rate and correlations with application to drug dissolution," AIChE Journal 65, e16617 (2019).
- 10. N. A. Frankel, and A. Acrivos, "Heat and mass transfer from small spheres and cylinders freely suspended in shear flow," The Physics of Fluids **11**, 1913 (1968).
- 11. A. Acrivos, "Heat transfer at high Peclet number from a small sphere freely rotating in a simple shear field," Journal of fluid mechanics **46**, 233 (1971).
- 12. G. Batchelor, "Mass transfer from a particle suspended in fluid with a steady linear ambient velocity distribution," Journal of fluid mechanics **95**, 369 (1979).
- 13. A. Polyanin, and V. Dil'man, "New methods of the mass and heat transfer theory—II. The methods of asymptotic interpolation and extrapolation," International Journal of Heat and Mass Transfer 28, 45 (1985).
- 14. G. Subramanian, and D. Koch, "Centrifugal forces alter streamline topology and greatly enhance the rate of heat and mass transfer from neutrally buoyant particles to a shear flow," Physical review letters **96**, 134503 (2006).
- 15. G. Subramanian, and D. L. Koch, "Inertial effects on the transfer of heat or mass from neutrally buoyant spheres in a steady linear velocity field," Physics of Fluids **18**, 073302 (2006).
- 16. W. Zhong, A. Yu, X. Liu, Z. Tong, and H. Zhang, "DEM/CFD-DEM modelling of non-spherical particulate systems: theoretical developments and applications," Powder technology **302**, 108 (2016).
- 17. W. Zhong, A. Yu, G. Zhou, J. Xie, and H. Zhang, "CFD simulation of dense particulate reaction system: Approaches, recent advances and applications," Chemical Engineering Science **140**, 16 (2016).

- 18. M. Masaeli, E. Sollier, H. Amini, W. Mao, K. Camacho, N. Doshi, S. Mitragotri, A. Alexeev, and D. Di Carlo, "Continuous inertial focusing and separation of particles by shape," Physical Review X 2, 031017 (2012).
- 19. P. Decuzzi, R. Pasqualini, W. Arap, and M. Ferrari, "Intravascular delivery of particulate systems: does geometry really matter?," Pharmaceutical research **26**, 235 (2009).
- 20. G. B. Jeffery, "The motion of ellipsoidal particles immersed in a viscous fluid," Proceedings of the Royal Society of London. Series A, Containing papers of a mathematical and physical character **102**, 161 (1922).
- 21. E.-J. Ding, and C. K. Aidun, "The dynamics and scaling law for particles suspended in shear flow with inertia," Journal of fluid mechanics **423**, 317 (2000).
- 22. D. Qi, and L.-S. Luo, "Rotational and orientational behaviour of three-dimensional spheroidal particles in Couette flows," Journal of fluid mechanics 477, 201 (2003).
- 23. Z. Yu, N. Phan-Thien, and R. I. Tanner, "Rotation of a spheroid in a Couette flow at moderate Reynolds numbers," Physical review E **76**, 026310 (2007).
- 24. W. Mao, and A. Alexeev, "Motion of spheroid particles in shear flow with inertia," Journal of fluid mechanics **749**, 145 (2014).
- 25. T. Rosén, M. Do-Quang, C. Aidun, and F. Lundell, "The dynamical states of a prolate spheroidal particle suspended in shear flow as a consequence of particle and fluid inertia," Journal of fluid mechanics 771, 115 (2015).
- 26. N. K. Marath, and G. Subramanian, "The effect of inertia on the time period of rotation of an anisotropic particle in simple shear flow," Journal of fluid mechanics **830**, 165 (2017).
- 27. N. K. Marath, and G. Subramanian, "The inertial orientation dynamics of anisotropic particles in planar linear flows," Journal of fluid mechanics **844**, 357 (2018).
- 28. F. Lundell, and A. Carlsson, "Heavy ellipsoids in creeping shear flow: transitions of the particle rotation rate and orbit shape," Physical review E **81**, 016323 (2010).
- 29. N. R. Challabotla, C. Nilsen, and H. I. Andersson, "On rotational dynamics of inertial disks in creeping shear flow," Physics Letters A **379**, 157 (2015).
- 30. Z. Cui, L. Zhao, W.-X. Huang, and C.-X. Xu, "Stability analysis of rotational dynamics of ellipsoids in simple shear flow," Physics of Fluids **31**, 023301 (2019).
- 31. Y.-H. Qian, D. d'Humières, and P. Lallemand, "Lattice BGK models for Navier-Stokes equation," EPL (Europhysics Letters) 17, 479 (1992).
- 32. S. Chen, and G. D. Doolen, "Lattice Boltzmann method for fluid flows," Annual review of fluid mechanics **30**, 329 (1998).
- 33. Y. Wang, J. G. Brasseur, G. G. Banco, A. G. Webb, A. C. Ailiani, and T. Neuberger, Development of a lattice-Boltzmann method for multiscale transport and absorption with application to intestinal function (Springer, 2010).
- 34. P. L. Bhatnagar, E. P. Gross, and M. Krook, "A model for collision processes in gases. I. Small amplitude processes in charged and neutral one-component systems," Physical review **94**, 511 (1954).
- 35. P. Lallemand, and L.-S. Luo, "Lattice Boltzmann method for moving boundaries," Journal of Computational Physics **184**, 406 (2003).
- 36. A. J. Ladd, "Numerical simulations of particulate suspensions via a discretized Boltzmann equation. Part 1. Theoretical foundation," Journal of fluid mechanics **271**, 285 (1994).
- 37. M. h. Bouzidi, M. Firdaouss, and P. Lallemand, "Momentum transfer of a Boltzmann-lattice fluid with boundaries," Physics of Fluids 13, 3452 (2001).

- 38. C. K. Aidun, Y. Lu, and E.-J. Ding, "Direct analysis of particulate suspensions with inertia using the discrete Boltzmann equation," Journal of fluid mechanics **373**, 287 (1998).
- 39. D. Frenkel, and M. Ernst, "Simulation of diffusion in a two-dimensional lattice-gas cellular automaton: a test of mode-coupling theory," Physical review letters **63**, 2165 (1989).
- 40. C. Lowe, and D. Frenkel, "The super long-time decay of velocity fluctuations in a two-dimensional fluid," Physica A: statistical mechanics and its applications **220**, 251 (1995).
- 41. R. Merks, A. Hoekstra, and P. Sloot, "The moment propagation method for advection—diffusion in the lattice Boltzmann method: validation and Péclet number limits," Journal of Computational Physics **183**, 563 (2002).
- 42. O. Filippova, and D. Hänel, "Grid refinement for lattice-BGK models," Journal of Computational Physics **147**, 219 (1998).
- 43. D. Yu, R. Mei, and W. Shyy, "A multi block lattice Boltzmann method for viscous fluid flows," International journal for numerical methods in fluids **39**, 99 (2002).
- 44. D. R. Mikulencak, and J. F. Morris, "Stationary shear flow around fixed and free bodies at finite Reynolds number," Journal of fluid mechanics **520**, 215 (2004).
- 45. K. Stewartson, "On almost rigid rotations," Journal of fluid mechanics 3, 17 (1957).
- 46. A. Van de Vooren, "The Stewartson layer of a rotating disk of finite radius," Journal of engineering mathematics **26**, 131 (1992).
- 47. R. Hollerbach, "Instabilities of the Stewartson layer Part 1. The dependence on the sign of," Journal of fluid mechanics **492**, 289 (2003).